Research Square

Preprints are preliminary reports that have not undergone peer review.
They should not be considered conclusive, used to inform clinical practice,
or referenced by the media as validated information.

Graphene-Regulated K-Ion Transport in Hierarchically Porous Biomass-Derived Carbon for High-Power Aqueous Supercapacitors

Taeyoung Park
Kongju National University
Hee Seung Eom
Kongju National University
Jeaeum Jin
Kongju National University
So yeon An
Kongju National University
Bo Young Yoon
Kongju National University
Ryunkyoung Lee
Kongju National University
Do Kyoung Han
Korea Basic Science Institute
Jong Seob Choi
Kongju National University
Dong Ju Lee
Chungbuk National University
Cheng Ai Li
Kongju National University
Sung Ho Song
shsong805@kongju.ac.kr

Kongju National University

Research Article

Keywords: Biomass-derived carbon, Graphene, Potassium-ion transport, Hierarchically porous carbon, Electric double-layer capacitor, Aqueous supercapacitor

Posted Date: November 10th, 2026

DOI: https://doi.org/10.21203/rs.3.rs-11441427/v1

License: This work is licensed under a Creative Commons Attribution 4.0 International License.
Read Full License

Additional Declarations: No competing interests reported.

Graphene-Regulated K-Ion Transport in Hierarchically Porous Biomass-Derived Carbon for High-Power Aqueous Supercapacitors

Taeyoung Park[1] · Hee Seung Eom[1] · Jeaeum Jin[1] · So Yeon An[1] · Bo Young Yoon[1] · Ryunkyoung Lee[1] · Do Kyoung Han[2] · Jong Seob Choi[1] · Dong Ju Lee[3,*] · Cheng Ai Li[1,*] · Sung Ho Song[1,*]

Taeyoung Park and Hee Seung Eom contributed equally to this work.

[*] Dong Ju Lee
E-mail: dongjulee@chungbuk.ac.kr

[*] Cheng Ai Li
E-mail: lca12@kongju.ac.kr

[*]Sung Ho Song
E-mail: shsong805@kongju.ac.kr

[1] Division of Advanced Materials Engineering, Kongju National University, Cheonan-si 31080, Republic of Korea

[2] Division of Materials Analysis and Research, Korea Basic Science Institute, 169–148, Gwahak-ro, Yuseong-Gu, Daejeon 34133, Republic of Korea
Department of Chemistry, Chung-Ang University, Seoul 06974, Republic of Korea

[3] Department of Urban, Energy, and Environmental Engineering, Chungbuk National University, Cheongju 28644, Republic of Korea

Abstract

Understanding how graphitic structures evolve in biomass-derived carbon and regulate ion transport is critical for designing high-power aqueous supercapacitors. However, the evolution of graphene-like domains during chemical activation of biomass-derived carbons and their subsequent influence on ion-specific charge-storage kinetics remain poorly understood. This study elucidates the activation-induced evolution of graphene-like domains in hierarchically porous carbon derived from balsa wood and establishes their role in regulating electrolyte-dependent ion storage. Structural evolution during activation involves the selective removal of disordered sp^3-rich carbon and K-mediated intercalation/exfoliation, followed by liquid-phase-assisted reconstruction of exfoliated graphitic sheets into extended graphene-like layers at 900 °C. In neutral K_2SO_4, the optimized *Act*.900 electrode maintains an energy density of 9.4 Wh kg^{-1} even at a high power density of 21.1 kW kg^{-1}, demonstrating its rapid charge-storage capability. Comparative electrochemical analysis using Li^+, Na^+, and K^+ electrolytes reveals a distinct K^+ advantage under high-rate conditions, arising from its low hydration energy, rapid desolvation, and favorable interaction with graphene interlayers. Electrodes with different degrees of graphene evolution further demonstrate

that continuous graphene-like domains critically regulate high-rate K-ion storage, providing a mechanistic basis for designing biomass-derived high-power aqueous supercapacitors.

Keywords Biomass-derived carbon · Graphene · Potassium-ion transport · Hierarchically porous carbon · Electric double-layer capacitor · Aqueous supercapacitor

1 Introduction

Electrochemical supercapacitors have emerged as promising energy-storage devices because of their rapid charge/discharge capability, high power density, and long cycling life.[1, 2] Among them, electric double-layer capacitors (EDLCs) store charge through reversible ion adsorption at the electrode/electrolyte interface, enabling exceptional power delivery and electrochemical stability.[3] However, their relatively low energy density remains a major limitation. Consequently, developing electrode architectures that simultaneously promote rapid ion transport and efficient charge storage has become a key objective for next-generation high-power supercapacitors. Porous carbon materials are the most widely investigated electrode materials for EDLCs because their interconnected pore networks provide efficient ion-transport pathways and large electrochemically accessible surface areas.[4, 5] Among the various porous carbon materials, biomass-derived carbons have emerged as particularly attractive candidates owing to their sustainability and naturally evolved hierarchical architectures.[6, 7] In particular, wood possesses highly aligned cellular channels that serve as an ideal structural template for constructing hierarchically porous carbon frameworks.[8-10] Nevertheless, optimizing pore architecture alone is insufficient to maximize high-rate electrochemical performance. Under rapid polarization, efficient charge storage requires the simultaneous transport of ions and electrons.

Accordingly, various graphitic domains, including graphene, reduced graphene oxide, and carbon nanotubes, have been incorporated into porous carbon electrodes to enhance electrical conductivity and maximize electrochemically active surface area.[5, 11-14] However, these graphitic domains have generally been regarded as passive conductive frameworks, while their influence on electrolyte-dependent ion transport has received far less attention. Beyond providing efficient electron transport pathways, graphitic domains also create well-defined graphitic interfaces that can directly interact with electrolyte ions during charge storage. This interfacial role is expected be particularly important in neutral aqueous potassium-ion supercapacitors, where charge-storage kinetics are governed by the coupled processes of ion diffusion, desolvation, and interfacial ion accommodation. Although K^+ possesses high ionic mobility, low hydration energy, and fast desolvation kinetics, the mechanism by which graphene-like graphitic domains regulate electrolyte-dependent K-ion transport remains largely unexplored. Establishing this structure–ion transport relationship is therefore essential for designing high-power biomass-derived supercapacitors.

Herein, we report a hierarchically porous graphitic carbon containing graphene-like layered domains synthesized from balsa wood through sequential delignification, carbonization, and KOH activation. By systematically correlating structural evolution with electrochemical behavior in Li^+, Na^+, and K^+ electrolytes, we demonstrate that graphene-like layered domains function not merely as conductive networks but as active regulators of electrolyte-dependent K-ion transport under rapid polarization. The optimized *Act*.900 architecture synergistically integrates hierarchical ion-transport pathways with continuous graphene-like layered domains,

thereby simultaneously promoting rapid electrolyte diffusion, efficient electron transport, and favorable K-ion accommodation. Comparative studies using electrodes with different degrees of graphene evolution establish a direct structure–ion transport–electrochemical performance relationship, revealing that the continuity of graphene-like domains governs high-rate K-ion storage. These findings provide mechanistic insight into graphene-regulated charge storage and establish a rational design principle for biomass-derived high-power aqueous supercapacitors. Unlike conventional strategies that simply improve conductivity by introducing graphitic carbon, this work reveals that graphene-like layered domains actively regulate K-ion transport and ultimately determine high-rate electrochemical performance.

2 Experimental Section

Fabrication of Hierarchically Porous Carbon Balsa wood (LLC, Loveland, CO, USA) was used as the biomass precursor for the preparing of hierarchically porous activated carbon. The wood was cut into rectangular pieces ($30 \times 70 \times 2$ mm^3) and dried at 70 °C for 24 h. Delignification was carried out by immersing the dried specimens in aqueous solution of 2.5 M NaOH (Samchun Pure Chemical, Korea) and 0.4 M Na_2SO_3 (Daejung Reagents Chemicals, Korea) for 6 h. The delignified wood was subsequently bleached in a 1:1 (v/v) mixture of H_2O_2 and deionized (DI) water at 80 °C for 1 h. The resulting cellulose-rich scaffolds were rinsed with ethanol and subjected to ultrasonication for 10 min; this procedure was repeated three times. The samples were then dryed at 70 °C. Carbonization were performed in a tubular furnace under flowing Ar by heating the samples to 800 °C at 15 °C min^{-1} and holding at this temperature for 1 h. The carbonized wood was subsequently mixed with KOH (Daejung Chemicals & Metals Co., Ltd., Korea) at a carbon/KOH mass ratio of 1:2. Chemical activation was conducted under Ar at 800, 900, or 1000 °C using the same heating rate of 15 °C min^{-1}. The resulting samples are denoted *Act*.800, *Act*.900, and *Act*.1000 according to the activation temperature.

Preparation of Aqueous Electrolytes Aqueous electrolytes solutions (1 M) were prepared by dissolving Li_2SO_4 (99.5%, Sigma-Aldrich), Na_2SO_4 (99.5%, Samchun Pure Chemical, Korea), or K_2SO_4 (99.0%, Samchun Pure Chemical, Korea) in DI water. The solutions were stirred at room temperature for 1 h until complete dissolution.

Structural and Chemical Characterization Surface morphology was examined by field-emission scanning electron microscopty (FE-SEM, XL30SFEG, Philips, Netherlands). The nanoscale carbon structure and graphitic layered domains were investigated by high-resolution transmission electron microscopy (HRTEM, Tecnai G2 F30, FEI, USA). For TEM measurements, powdered samples were dispersed in ethanol and deposited onto carbon-coated Cu grids. Surface elemental composition and carbon bonding states were analyzed by X-ray photoelectron spectroscopy (XPS, Sigma Probe, Thermo Fisher Scientific, USA). Raman spectra (N8 Senterra, Bruker GmbH, Germany) was used to evaluate the structural ordering and defect characteristics of the carbon meterials.

Electrochemical Measurements Working electrodes were prepared from a mixture containing 85 wt% active material, 10 wt% Super P conductive carbon (Alfa Aesar, UK), and 5 wt% poly(vinylidene fluoride) (Sigma-Aldrich). *N*-methyl-2-pyrrolidone (Daejung Chemical & Metals Co., Ltd., Korea) was added to form a homogeneous slurry, which was coated onto a current collector to a thickness of ≈25 μm and dried at 80 °C for 1 h. Electrochemical measurements were performed in a symmetric two-electrode cell (PAT-Cell, EL-CELL,

Germany) using an SP-150 potentiostat/galvanostat (BioLogic, France). The cells were evaluated in 1 M aqueous Li_2SO_4, Na_2SO_4, and K_2SO_4 electrolytes. Cyclic voltammetry (CV) was conductd over 0–0.8 V at scan rates of 10–500 mV s^{-1}. Galvanostatic charge–discharge (GCD) measurements were performed within the sampe voltage window at current densities ranging from 0.1 to 5 A g^{-1}. Electrochemical impedance spectroscopy (EIS) were recorded conducted at open-circuit voltage over frequency range of 100 kHz –100 MHz using a AC amplitude of 10 mV. The specific capacitance, C, was determined from the CV measurements according to

$$C = \frac{2\int I\,dV}{mv\Delta V} \quad (1)$$

where $\int I\,dV$ is the integrated CV area, m is the total mass of the electrode, v is the scan rate, ΔV is the operating voltage window, I is the discharge current, and Δt is the discharge time.

The specific energy density (E) and power density (P) were calculated as

$$E = C\,(\Delta V)^2 / 8 \quad (2)$$

and

$$P = I\,\Delta V / (2m) \quad (3)$$

respectively.

3 Results and Discussion

The structural evolution of balsa wood during the fabrication of hierarchically porous graphitic carbon is illustrated in Fig. 1. The synthetic strategy integrates sequential delignification, carbonization, and KOH activation to progressively transform the native wood architecture into a conductive porous carbon framework while preserving its intrinsic anisotropic morphology. FE-SEM observations reveal the structural evolution throughout each processing step (Fig. 1b–e). Pristine balsa wood exhibits a highly ordered cellular architecture composed of thick cell walls and well-aligned longitudinal channels (Fig. 1b). Following delignification and bleaching, most lignin and hemicellulose are selectively removed, leaving behind a cellulose-dominated scaffold with substantially thinned cell walls and enlarged luminal spaces (Fig. 1c). Importantly, despite the extensive removal of amorphous matrix components, the continuous cellular framework remains structurally intact. This robust cellulose template provides an ideal structural precursor for preserving the macroscopic wood architecture during subsequent thermal conversion. After carbonization at 800 °C, the anisotropic channel network is largely retained while the cellulose framework is transformed into an electrically conductive carbon skeleton (Fig. 1d). The minimal structural collapse observed after pyrolysis demonstrates that the preformed cellulose scaffold effectively maintains the three-dimensional architecture throughout carbonization. Such structural preservation is advantageous for constructing continuous ion-transport pathways in the final electrode. Subsequent KOH activation generates abundant nanoscale porosity while preserving the inherited cellular framework (Fig. 1e). Under appropriate activation conditions, hierarchical pores and graphene-like graphitic domains are simultaneously developed, establishing a conductive porous architecture for rapid ion transport. The integration of hierarchical pore networks with graphitic conductive pathways therefore establishes the structural basis for rapid ion diffusion and efficient charge storage, which are examined in the following electrochemical studies.

The influence of activation conditions on the structural evolution of the biomass-derived carbon was systematically investigated using SEM and HRTEM analyses (Fig. 2). Samples activated at 800, 900, and 1000 °C were prepared using a fixed carbon-to-KOH mass ratio of 1:2 to elucidate the effect of activation temperature on

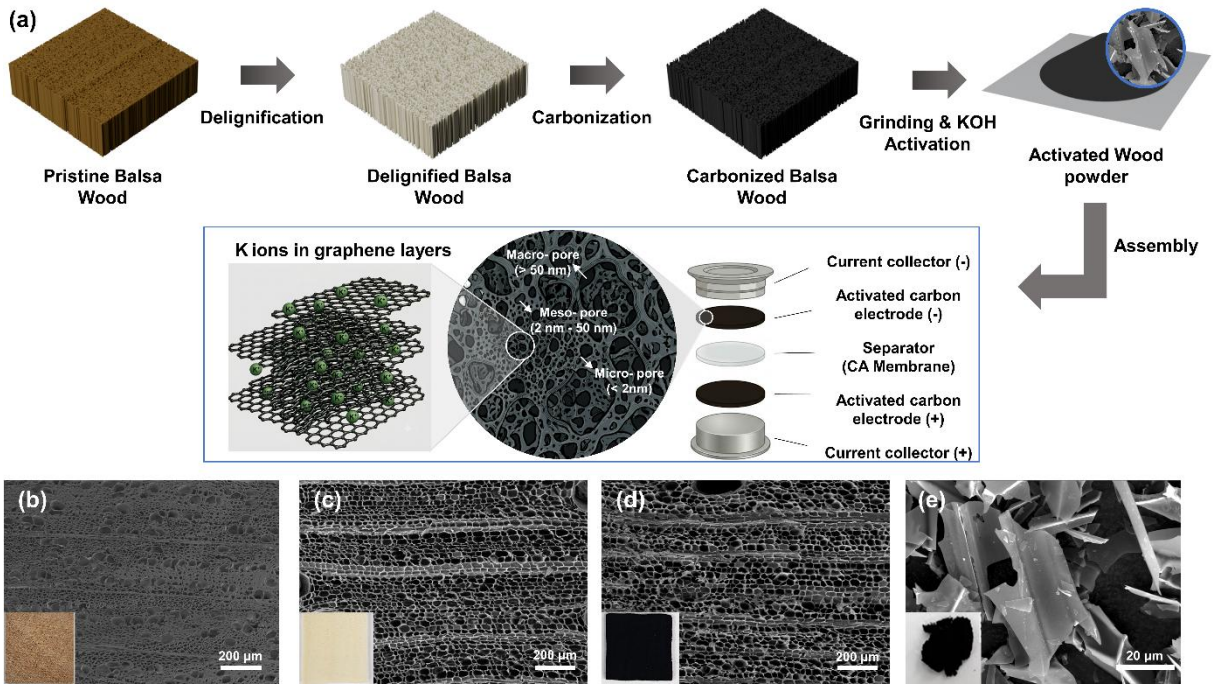


Fig. 1 (a) Schematic illustration of the fabrication process from pristine balsa wood to activated balsa wood powder, followed by assembly of a two-electrode supercapacitor incorporating K-ion-intercalated graphene layers within the hierarchically porous carbon. SEM images and corresponding inset photographs of (b) pristine balsa wood, (c) delignified balsa wood, (d) carbonized balsa wood, and (e) activated balsa wood powder.

the morphology and carbon microstructure. SEM observations primarily reveal the preservation and evolution of the overall carbon framework during activation (Fig. 2a–c). The *Act.*800 sample retained a relatively dense platelet-like morphology with smooth surfaces, indicating that structural modification remained limited under the relatively mild activation condition (Fig. 2a). Increasing the activation temperature to 900 °C produced a noticeably rougher carbon surface while preserving the integrity of the platelet framework (Fig. 2b), suggesting that the activation reaction proceeded uniformly without causing structural collapse. In contrast, the *Act.*1000 sample exhibited severe framework deterioration accompanied by enlarged voids and fragmented carbon plates (Fig. 2c), indicating excessive carbon consumption under harsh activation conditions. These observations demonstrate that the activation temperature primarily governs the balance between framework preservation and carbon etching.

The internal microstructure was further examined by TEM to elucidate the evolution of graphitic ordering during activation (Fig. 2d–i). The *Act.*800 sample exhibited only locally developed graphene-like layers embedded within a predominantly disordered carbon matrix (Fig. 2d and g), indicating that graphitic reconstruction remained limited under the relatively mild activation condition. In contrast, the *Act.*900 sample displayed extensive graphene-like layered domains with relatively continuous stacking throughout the carbon framework (Fig. 2e and h). The coexistence of well-preserved porous architecture and highly ordered graphitic layers suggests that activation at 900 °C provides an optimal balance between structural preservation and graphitic reconstruction. Further increasing the activation temperature to 1000 °C resulted in fragmentation of the layered domains together with the appearance of predominantly amorphous carbon regions (Fig. 2f and i), indicating that excessive activation progressively disrupts the sp^2 carbon network despite continued carbon etching. These observations identify 900 °C as the optimal activation temperature for simultaneously developing hierarchical porosity and graphene-

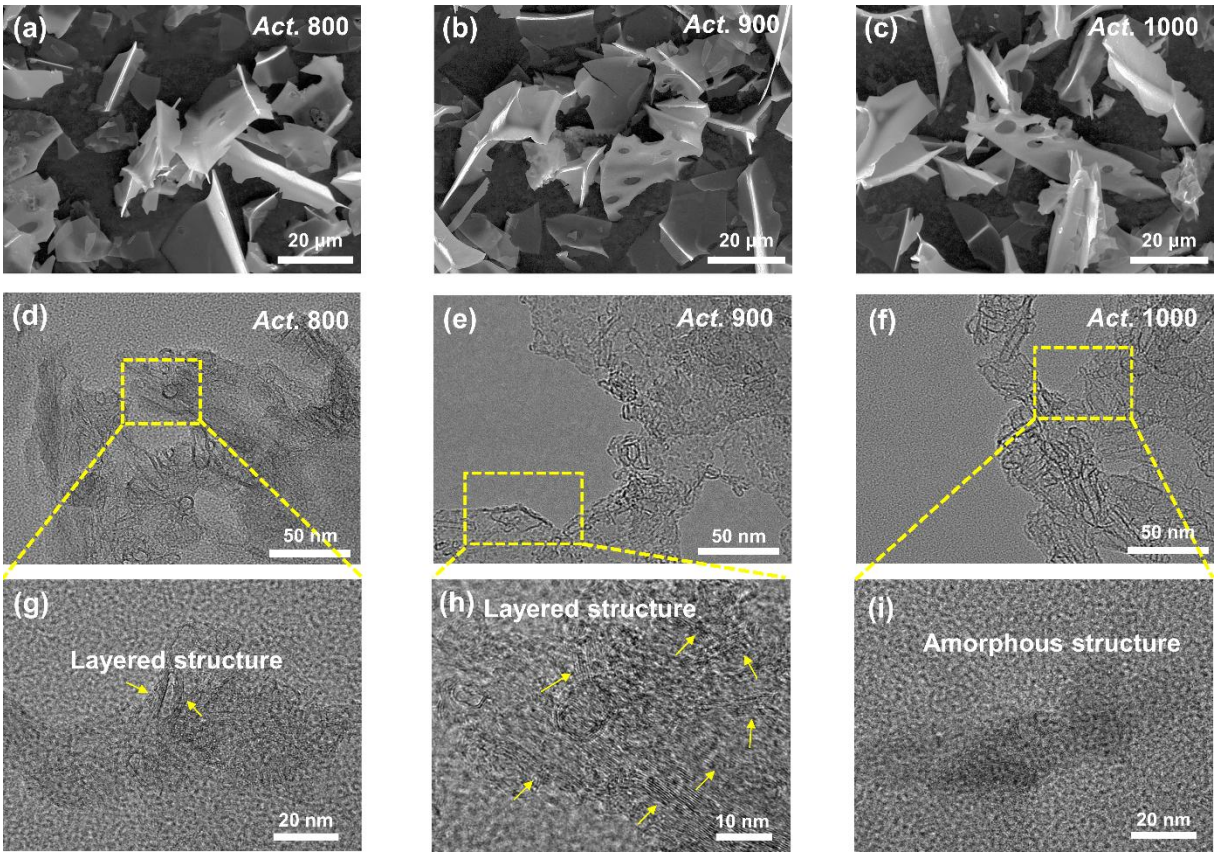


Fig. 2 SEM images of *Act.*800, *Act.*900, and *Act.*1000 at (a–c), respectively. Low-magnification TEM images of (d–f) and corresponding high-magnification TEM images of (g–i).

like layered domains, thereby establishing the structural basis for the activation mechanism discussed in the following section.

To further verify the structural reconstruction induced by KOH activation, Raman spectroscopy and XPS were employed to investigate graphitic ordering and carbon bonding configurations (Fig. 3). Raman spectra of all activated samples exhibit the characteristic D (~1350 cm^{-1}) and G band (~1580 cm^{-1}), corresponding to defect-induced carbon and graphitic sp^2 carbon, respectively (Fig. 3a). The I_D/I_G ratio remained nearly unchanged (0.97–1.01) regardless of activation temperature, indicating that KOH activation does not substantially increase the overall defect density of the carbon framework. Instead, the G band shifted from 1576 cm^{-1} for carbonized wood to 1587 cm^{-1} after activation at 800 and 900 °C, suggesting progressive ordering of the sp^2 carbon network.[15] Upon further increasing the activation temperature to 1000 °C, the G band slightly shifted back to 1584 cm^{-1}, implying partial disruption of the graphitic lattice caused by overactivation. More importantly, *Act.*900 exhibits the most intense 2D band among all samples, providing strong evidence for the formation of extended graphene-like layered domains.[16] This interpretation is fully consistent with the TEM observations (Fig. 2), where *Act.*900 displays continuous graphene-like sheets with relatively ordered stacking, whereas *Act.*800 contains only locally developed graphitic layers and *Act.*1000 exhibits fragmented graphene domains embedded within an amorphous carbon matrix. Although the overall defect density remained nearly unchanged, the weakened 2D band together with the slight downshift of the G band at 1000 °C indicates that excessive activation fragments the graphene-like domains rather than promoting further graphitic reconstruction.

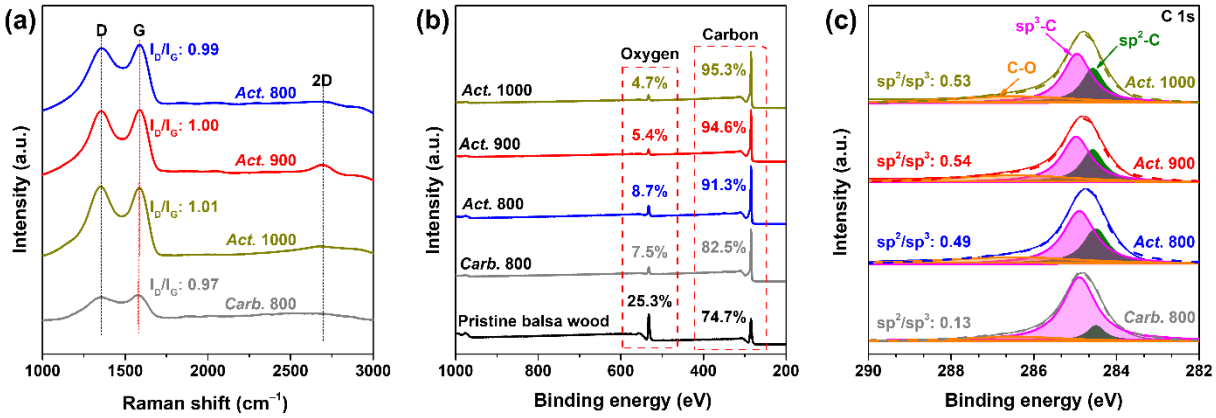


Fig. 3 (a) Raman spectra of carbonized wood (*Carb*.800) and activated carbons (*Act*.800, *Act*.900, and *Act*.1000). (b) XPS survey spectra and (c) high-resolution C 1s spectra of pristine balsa wood, *Carb*.800, *Act*.800, *Act*.900, and *Act*.1000.

The evolution of carbon bonding was further examined by XPS (Fig. 3b and c). Survey spectra revealed comparable elemental compositions among the activated samples, with carbon contents of 95.3%, 94.6%, and 93.1% for *Act*.800, *Act*.900, and *Act*.1000, respectively. High-resolution C 1s spectra were deconvoluted into sp^2 carbon (284.5 eV), sp^3 carbon (284.9 eV), and C–O species (286.3 eV).[17] Before activation, carbonized wood was dominated by sp^3-hybridized carbon, exhibiting a low sp^2/sp^3 ratio of only 0.13. This result indicates that the carbonized framework primarily consists of graphite microcrystals interconnected by an amorphous sp^3-rich carbon matrix, which is characteristic of hard carbon derived from partially carbonized cellulose. Following KOH activation, the relative contribution of sp^2 carbon increased markedly at the expense of the sp^3 component, confirming progressive graphitic reconstruction. Notably, the sp^2/sp^3 ratio reached 0.54 for Act.900 and remained nearly unchanged (0.53) for Act.1000. This observation suggests that excessive activation does not significantly reduce the overall fraction of sp^2-bonded carbon. Instead, when considered together with the Raman and TEM results, it indicates that overactivation primarily disrupts the continuity of graphene-like domains rather than decreasing the total amount of sp^2 carbon. Taken together, TEM directly visualizes the evolution of graphene-like layered domains, Raman spectroscopy reveals the temperature-dependent development of graphitic ordering, and XPS demonstrates the conversion of amorphous sp^3 carbon into graphitic sp^2 carbon. The excellent agreement among these complementary characterization techniques indicates that KOH activation promotes graphitic reconstruction in a temperature-dependent manner rather than merely generating porosity.

Based on the structural and spectroscopic observations, the mechanism for the evolution of graphene-like domains during KOH activation is proposed in Fig. 4. The carbonized wood initially consists of graphitic microcrystals embedded within a relatively disordered, sp^3-rich carbon matrix. Upon heating, KOH undergoes a series of thermochemical reactions with the carbon matrix, generating H_2, CO, CO_2, K_2CO_3, K_2O, and metallic K (Equations (4)–(9)).[18-21] KOH first dehydrates to form K_2O and H_2O, and the released H_2O can subsequently react with carbon to produce CO and H_2. Concurrently, direct reactions between KOH and carbon generate K_2CO_3 and metallic K. As the temperature increases, KOH is progressively converted into K_2CO_3, which can subsequently form K_2O and CO_2. Both K_2CO_3 and K_2O further react with carbon, sustaining the generation of metallic K while progressively consuming the more reactive disordered carbon phase.[22]

$$2KOH \rightarrow K_2O + H_2O \quad (4)$$

$$C + H_2O \rightarrow CO + H_2 \quad (5)$$

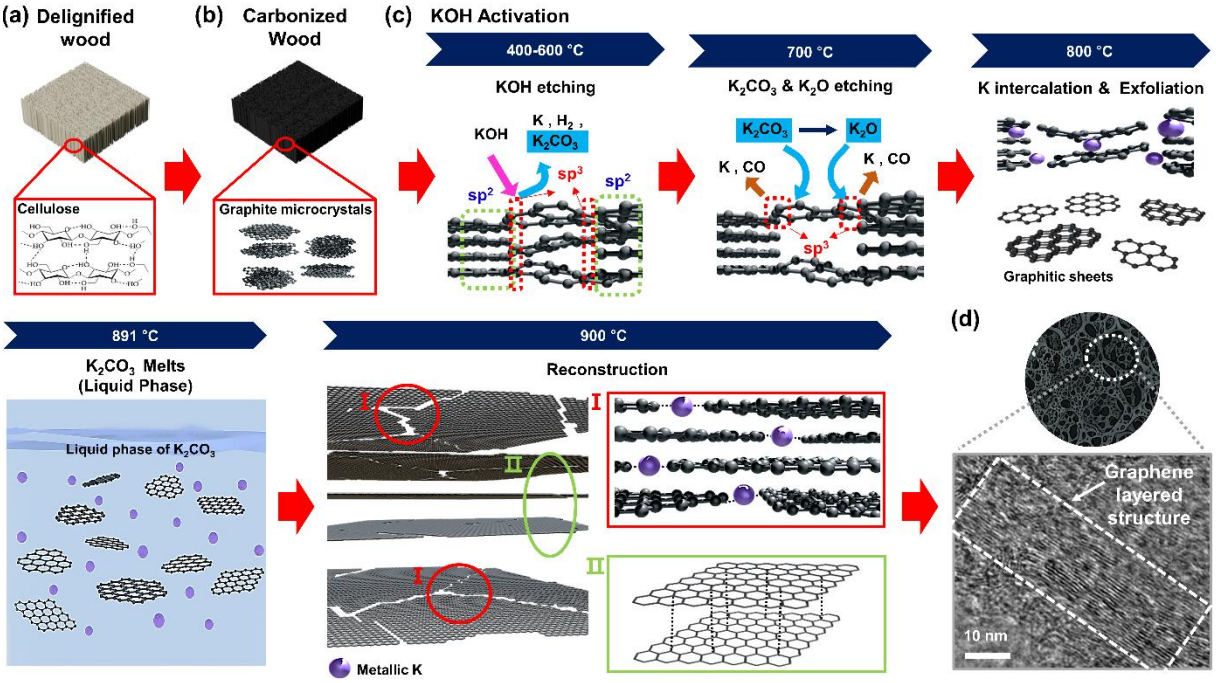


Fig. 4 Proposed mechanism for the activation-induced evolution of graphene-like domains in biomass-derived carbon. (a) Cellulose-rich delignified wood. (b) Carbonized wood containing graphitic microdomains embedded within a disordered carbon matrix. (c) During KOH activation, selective removal of disordered carbon and metallic K-mediated intercalation/exfoliation progressively liberate graphitic microdomains, followed by liquid-phase-assisted reconstruction into extended graphene-like domains above the melting point of K_2CO_3. (d) Schematic representation of the resulting hierarchically porous carbon with graphene-like domains and the corresponding high-resolution TEM image of *Act*.900.

$$6KOH + 2C \rightarrow 2K + 3H_2 + 2K_2CO_3 \quad (6)$$

$$K_2CO_3 \rightarrow K_2O + CO_2 \quad (7)$$

$$K_2CO_3 + 2C \rightarrow 2K + 3CO \quad (8)$$

$$K_2O + C \rightarrow 2K + CO \quad (9)$$

Because the less ordered sp^3-rich carbon is more susceptible to chemical activation than the graphitic sp^2 domains, these reactions preferentially consume the disordered carbon matrix and progressively remove the sp^3-rich carbon bridges connecting the pre-existing graphitic microcrystals. Removal of these bridges releases the graphitic microcrystals from the surrounding amorphous matrix, allowing their subsequent separation and structural rearrangement during high-temperature activation. Simultaneously, metallic K generated *in situ* can intercalate bewteen graphitic layers, increasing the interlayer spacing and weakening the interactions between adjacent carbon sheets. This K intercalation can further promote expansion and exfoliation of the layered carbon structure.[21] These processes are consistent with the locally develped graphene-lke layers observed in *Act*.800. A pronounced structural transition occurs at 900 °C, above the melting point of K_2CO_3 (≈891 °C). The resulting liquid-phase activation environment is expected to enhance the mobility of K-containing species and facilitate the rearrangement of liberated sp^2-rich graphitic.[22] Metallic K further assist this reconstruction through transient intercalation and charge-transfer interactions with the carbon framework.[20] Together, these processes promote the reorganization and coalescence of smaller graphitic domains into larger and more continuous graphene-like layers. Consequently, *Act*.900 exhibits the most developed layered architecture among the investigated samples,

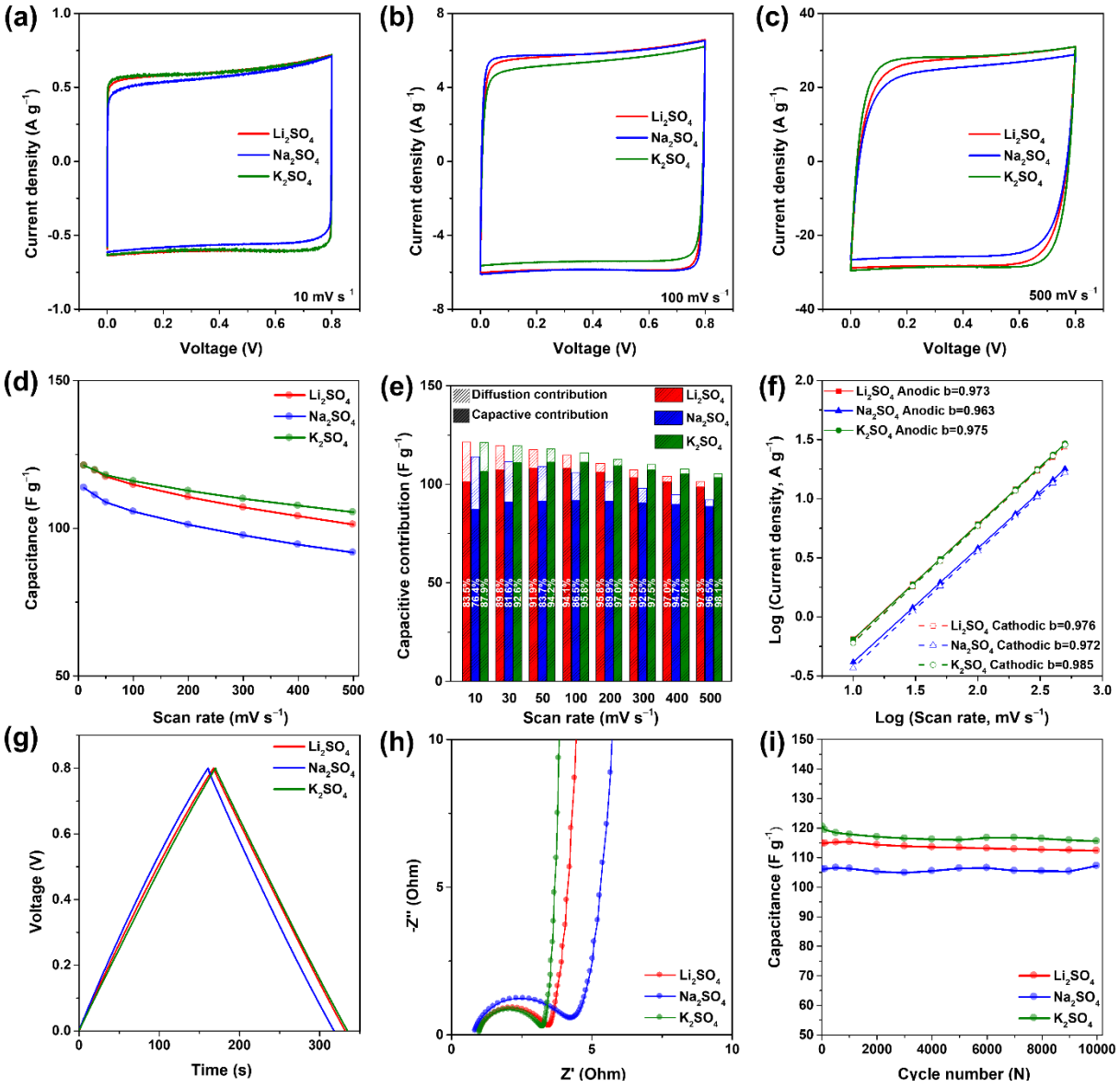


Fig. 5 Electrochemical performance and charge-storang kinetics of *Act*.900 in 1 M Li_2SO_4, Na_2SO_4, and K_2SO_4 electrolytes. (a–c) CV curves recorded at scan rates of (a) 10, (b) 100, and (c) 500 mV s^{-1}. (d) Specific capacitance as a function of scan rate. (e) Capacitive contribution analysis at different scan rates. (f) Determination of b values from the current response at 0.6 V. (g) GCD curves recorded at a current density of 0.3 A g^{-1} (h) Nyquist plots obtained from EIS. (i) Cycling stability over 10,000 CV cycles at a scan rate of 10 mV s^{-1}.

consistent with the pronounced 2D Raman feature, the increased sp^2/sp^3 ratio, and the well-resolved graphene-like domains observed by TEM. Further increasing the activation temperature to 1000 °C shifts the structural evolution toward excessive activation. Under these harsher activation conditions, the extended graphene-like layers become increasingly fragmented and lose their structural continuity, as supported by the TEM and Raman results. Thus, the proposed mechanism can be described as two sequential stages: below the melting point of K_2CO_3, preferential removal of disordered sp^3-rich carbon together with K-mediated intercalation and exfoliation releases and separates the pre-existing graphitic microdomains; once K_2CO_3 enters the molten state, the liquid-phase environment facilitates their structural rearrangement and coalescence, leading to the development of larger and more continuous graphene-like domains at *Act*.900.

The electrolyte-dependent electrochemical behavior of the optimized *Act*.900 electrode was systematically investigated in 1 M Li_2SO_4, Na_2SO_4, and K_2SO_4 aqueous electrolytes using CV, GCD, and EIS (Fig. 5). All electrolytes exhibited nearly rectangular CV profiles over the entire scan-rate range without discernible redox peaks, confirming that charge storage is dominated by electric double-layer capacitance rather than Faradaic reactions (Fig. 5a–c). The specific capacitances obtained at 10 mV s^{-1} were 121.3, 113.7, and 121.2 F g^{-1} for Li_2SO_4, Na_2SO_4, and K_2SO_4 electrolytes, respectively (Fig. 5d and Table S1). Although the three neutral electrolytes delivered comparable capacitances at low scan rates, their rate capability became increasingly differentiated under rapid polarization. At 500 mV s^{-1}, the capacitance retention reached 83.5%, 85.8%, and 87.0% for Li_2SO_4, Na_2SO_4, and K_2SO_4, respectively. Consequently, the capacitance sequence evolved from Na_2SO_4 < K_2SO_4 ≈ Li_2SO_4 at low scan rates to Na_2SO_4 < Li_2SO_4 < K_2SO_4 at high scan rates, indicating that electrolyte-dependent ion transport becomes increasingly important under high-rate operation.

The charge-storage kinetics of the *Act*.900 electrode were further quantified by separating the current response into capacitive and diffusion-controlled contributions according to

$$i(V)=k_1v+k_2v^{1/2} \quad (10)$$

where $i(V)$ is the current response at a given potential V, v is the scan rates, and k_1v and $k_2v^{1/2}$ represent the capacitive and diffusion-controlled contributions, respectively.[23, 24] As shown in Fig. 5e and S1, the capacitive contribution of the *Act.* 900 in K_2SO_4 was 87.9% at 10 mV s^{-1} and progressively increased to 98.1% at 500 mV s^{-1}. Notable, this value was higher than those obtained in Li_2SO_4 (97.3%) and Na_2SO_4 (96.5%) under the same high-rate condition. Moreover, K_2SO_4 maintained the highest capacitive contribution over the investigated scan-rate range, indicating that K^+ is less constrained by diffusion as the polarization rate increases. The kinetic characteristics were independently assessed using the power-law relationship

$$i = av^b \quad (11)$$

where a and b are adjustable parameters. A b-value approaching 1 indicates predominatly surface-controlled kinetics, whereas b = 0.5 is characteristic of a diffusion-controlled process.[24-26] The b-values obtained for all three electrolytes were close to unity (Fig. 5f), corroborating the predominantly capacitive nature of charge storage in *Act*.900. Together, the high capacitive contribution and near-unity b-values indicate rapid charge-storage kinetics with limited diffusion constraints. The consistently higher capacitive contribution in K_2SO_4 further supports the favorable high-rate K^+ response enabled by the hierarchical porous framework and graphene-like layered domains. The GCD profiles exhibited nearly symmetric triangular shapes with negligible IR drops (Fig. 5g), confirming excellent electrochemical reversibility. At 5 A g^{-1}, capacitance retention remained as high as 93.9%, 86.9%, and 95.5% for Li_2SO_4, Na_2SO_4, and K_2SO_4, respectively, demonstrating excellent rate capability under high-current operation (Fig. S2). Electrochemical impedance spectroscopy further revealed electrolyte-dependent interfacial kinetics (Fig. 5h). The charge-transfer resistance decreased in the order Na_2SO_4 (3.42 Ω) > Li_2SO_4 (2.45 Ω) > K_2SO_4 (2.26 Ω), consistent with the superior high-rate capacitive behavior observed in K_2SO_4 electrolyte. Long-term cycling stability was evaluated over 10,000 charge/discharge cycles (Fig. 5i). All electrolytes exhibited outstanding durability with capacitance retention exceeding 99.9%, including 99.98%, 99.99%, and 99.96% for Li_2SO_4, Na_2SO_4, and K_2SO_4, respectively, confirming the excellent structural robustness of the optimized graphitic porous electrode.

To elucidate the origin of the electrolyte-dependent rate performance, the intrinsic physicochemical properties of alkali-metal ions together with the structural characteristics of the graphitic porous framework were systematically considered (Fig. 6). The hydrated ionic radius decreases in the order Li^+–H_2O > Na^+–H_2O > K^+–

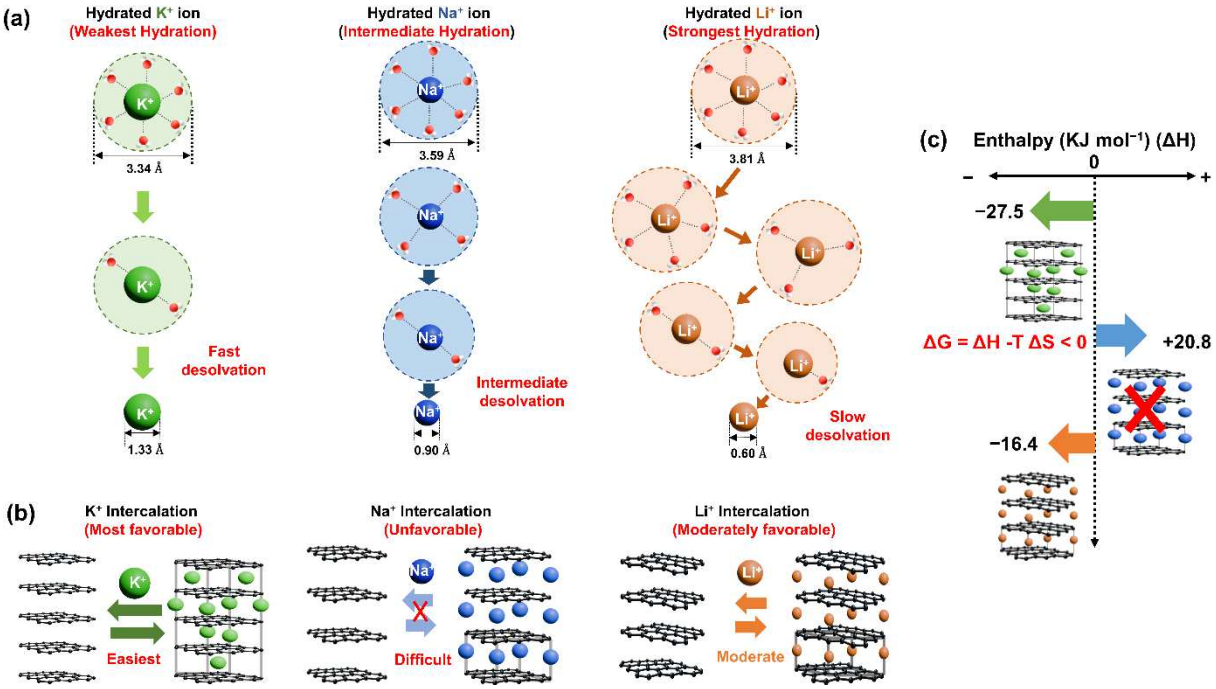


Fig. 6 Proposed mechanism for electrolyte-dependent ion transport and charge storage in graphene-like domains. (a) Hydrated K^+, Na^+, and Li^+ ions and their desolvation process. (b) Schematic illustration of K^+, Na^+, and Li^+ insertion/extraction within graphene-like layered domains during charge/discharge. (c) Reported intercalation enthalpies of KC_8, LiC_6, and NaC_6.[30]

H_2O, whereas ionic mobility and conductivity exhibit the opposite trend ($K^+ > Na^+ > Li^+$).[27, 28] These intrinsic ion properties directly govern ion diffusion, desolvation, and interfacial charge-transfer processes within the hierarchical porous electrode. Considering that the pore dimensions of the *Act*.900 electrode are substantially larger than the hydrated ion sizes, differences in hydrated ionic radius alone cannot fully explain the observed electrolyte-dependent electrochemical behavior. At relatively low scan rates, all alkali-metal ions have sufficient time to diffuse throughout the porous framework and access both the external pore surface and the graphene-like layered domains, resulting in comparable capacitance values. As the scan rate increases, however, charge-storage kinetics become increasingly limited by ion desolvation and interfacial transport. Owing to its lower hydration energy, weaker hydration shell, and higher ionic mobility, K^+ undergoes faster partial desolvation and can more readily access both the external pore surface and graphene interlayers, thereby preserving superior rate capability under rapid polarization.

Besides the kinetic advantage of K^+ transport, the interaction between alkali-metal ions and graphene-like layered domains also plays an important thermodynamic role. Thermodynamically, the feasibility of alkali metal intercalation into the graphitic lattice is fundamentally determined by the Gibbs free energy change ($\Delta G = \Delta H - T\Delta S$). Previous theoretical studies have demonstrated that K-ion intercalation into graphitic layers is energetically more favorable than Li-ion intercalation, whereas Na-ion intercalation remains thermodynamically unfavorable.[29, 30] The reported formation enthalpies of KC_8 (−27.5 kJ mol^{-1}), LiC_6 (−16.4 kJ mol^{-1}), and NaC_6 (+20.8 kJ mol^{-1}) clearly support this tendency.[30] This distinctly exothermic enthalpy of KC_8 decisively shifts the Gibbs free energy toward a negative regime ($\Delta G < 0$), validating that potassium intercalation into the carbon matrix is energetically favored and highly spontaneous. Consequently, the graphene-like layered domains provide additional ion-accessible galleries beyond the conventional external electric double-layer surface, preferentially

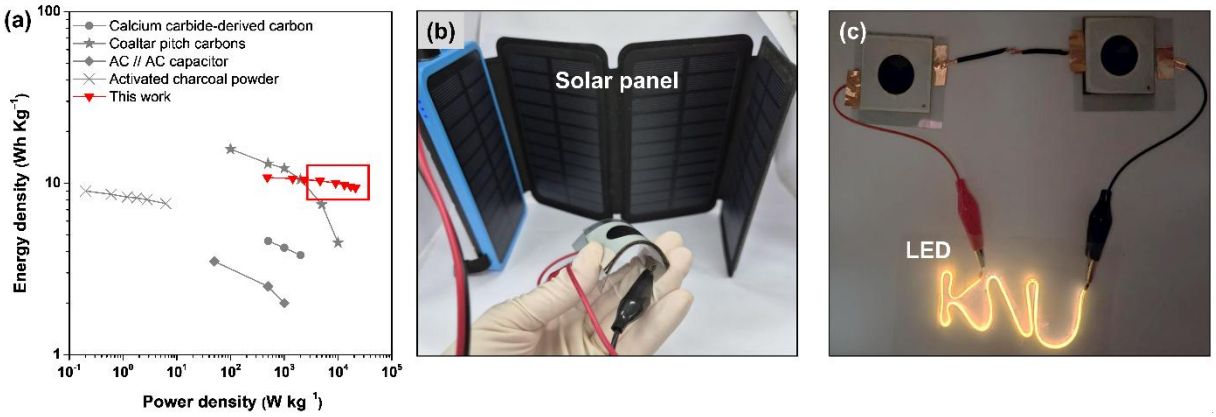


Fig. 7 (a) Ragone plot comparing the electrochemical performance of the Act.900 symmetric supercapacitor with previously reported calcium carbide-derived carbon, coal tar pitch-derived carbon, AC//AC, and activated charcoal supercapacitors operated in aqueous K_2SO_4 electrolyte.[31–34]. (b-c) Digital photographs demonstrating the charging of the flexible supercapacitor using a solar panel and the subsequent illumination of a "KNU" logo LED by the supercapacitors connected in series.

promoting reversible K-ion insertion/extraction during rapid charge/discharge processes. Accordingly, the outstanding high-rate performance observed in K_2SO_4 electrolyte originates from the synergistic combination of favorable ion-transport kinetics and thermodynamically preferred K-ion interaction with graphene-like layered domains.

To further clarify the role of graphene-like layered domains, the electrochemical response of the *Act*.800 electrode in K_2SO_4 electrolyte was additionally examined and compared with those of *Act*.900 and the overactivated *Act*.1000 electrode (Fig. S3 and S4). *Act*.800 delivered intermediate electrochemical performance between *Act*.900 and *Act*.1000 throughout the entire scan-rate range, consistent with the TEM observations showing partially developed graphene-like layers. In contrast, *Act*.900 contained continuous graphene-like layered domains, whereas *Act*.1000 exhibited fragmented graphitic structures caused by excessive activation. Notably, *Act*.1000 consistently exhibited the capacitance sequence $Li_2SO_4 > Na_2SO_4 > K_2SO_4$, with K_2SO_4 showing the poorest rate capability, in sharp contrast to the optimized *Act*.900 electrode. These results establish a clear structure–property relationship, demonstrating that the progressive evolution from partially developed graphene domains (*Act*.800) to continuous graphitic networks (*Act*.900), followed by structural fragmentation after overactivation (*Act*.1000), directly governs high-rate K-ion storage. Taken together, the superior rate capability of the *Act*.900 electrode originates from the synergistic integration of hierarchical pore architecture and continuous graphene-like layered domains. The hierarchical porous framework provides efficient electrolyte transport pathways, whereas the graphitic layers establish highly conductive electron pathways while simultaneously offering energetically favorable K-ion storage sites. Under rapid polarization, these structural advantages enable fast desolvation, efficient interfacial charge transfer, and reversible K-ion intercalation, thereby producing the outstanding high-rate electrochemical performance observed for the optimized biomass-derived carbon electrode.

Finally, the electrochemical performance of the optimized *Act*.900 electrode was benchmarked against previously reported aqueous K_2SO_4-based carbon supercapacitors using Ragone plots (Fig. 7). The present electrode delivered a maximum energy density of 10.8 Wh kg^{-1} at 485 W kg^{-1} while retaining 9.4 Wh kg^{-1} even at an ultrahigh power density of 21.1 kW kg^{-1}. Compared with representative carbon/graphene composites, carbide-derived carbons, coal-tar pitch carbons, and conventional activated-carbon electrodes reported in the

literature, the present electrode demonstrates one of the highest power densities while maintaining competitive energy density.[31-34] Although its energy density remains moderate relative to battery-type electrodes, the exceptional power capability highlights the effectiveness of coupling hierarchical porosity with graphene-like layered domains. Notably, only a slight decrease in energy density was observed as the power density increased, indicating highly efficient ion/electron transport within the graphitic porous framework. To further demonstrate the practical applicability of the developed supercapacitor as an energy storage device, a flexible supercapacitor was fabircated using *Act*.900-coated ITO/PET electrodes and integrated with a commercial solar panel to construct a solar-powered energy storage system. As shown in Fig. 7b and c, the flexible supercapacitor was charged using the solar panel and subsequently used to illuminate a "KNU" logo LED with two units connected in series. These results demonstrate that the optimized biomass-derived graphitic carbon is well suited for high-power aqueous K-ion supercapacitors, highlighting its potential for practical energy storage applications in solar-powered portable and flexible electronic devices.

4 Conclusion

In this work, hierarchically porous graphitic carbon containing graphene-like layered domains was successfully fabricated from balsa wood through sequential delignification, carbonization, and KOH activation. Optimizing the activation temperature at 900 °C produced an interconnected porous framework together with continuous graphene-like domains, enabling efficient electrolyte diffusion and rapid electron transport. As a result, the optimized *Act*.900 electrode exhibited outstanding electrochemical performance in neutral K_2SO_4 electrolyte, delivering high specific capacitance, excellent rate capability, and remarkable cycling stability. More importantly, systematic investigations using Li^+, Na^+, and K^+ electrolytes revealed that the superior high-rate performance originates from graphene-regulated K-ion transport. The hierarchical pore network provides efficient ion-accessible pathways, whereas graphene-like layered domains promote fast electron conduction and create energetically favorable sites for reversible K-ion intercalation. Owing to its lower hydration energy, faster desolvation kinetics, and favorable interaction with graphene layers, K^+ maintains more efficient interfacial charge transfer and charge-storage kinetics than Li^+ and Na^+. Furthermore, comparative studies using *Act*.800, *Act*.900, and *Act*.1000 establish a clear structure–property relationship, demonstrating that the continuity of graphene-like layered domains, rather than their mere presence, governs high-rate K-ion storage. Overall, this work demonstrates that engineering graphene-like layered domains within hierarchically porous biomass-derived carbon provides an effective strategy for regulating ion transport in aqueous supercapacitors. The mechanistic insights presented here establish a structure–ion transport–electrochemical performance relationship and offer a rational design principle for developing sustainable high-power K-ion aqueous supercapacitors.

Supplementary Information The online version contains supplementary material available at http://doi.org/x.

Author contribution The manuscript was written with contributions from all authors. The experiments were conceptualized by Dong Ju Lee, Cheng Ai Li and Sung Ho Song. The conduction of experiments and organization of data were performed by Taeyoung Park, Hee Seung Eom, Jeaeum Jin, So Yeon An, Bo Young Yoon, Ryunkyoung Lee, Do Kyoung Han, Jong Seob Choi. All authors contributed to the data analysis and discussion of the results. All authors have read and agreed to the published version of the manuscript.

Funding This research was supported by Basic Science Research Program through the National Research Foundation of Korea funded by the Ministry of Education (RS-2019-NR040074) and by the Ministry of Education (RS-2025-00558261). This research was also supported by the IITP (Institute of Information & Communications Technology Planning & Evaluation)-ITRC (Information Technology Research Center) (IITP-2025-RS-2024-00438335, 25%) grant funded by the Korea government (Mistry of Science and ICT). This research was supported by Korea Institute for Advancement of Technology (KIAT) grant funded by the Korea Government (MOTIE) (RS-2024-00410787, HRD Program for Industrial Innovation).

Acknowledgement

This work was supported by the Research year project of the Kongju National University in 2026.

Data availability No datasets were generated or analyzed during the current study.

Declarations

Competing interests The authors declare no competing interests.

References

1. Huang J, Xie Y, You Y, Yuan J, Xu Q, Xie H, Chen Y (2023) Rational Design of Electrode Materials for Advanced Supercapacitors: From Lab Research to Commercialization. Adv Funct Mater 33(14): 2213095. https://doi.org/10.1002/adfm.202213095
2. Iqbal MF, Nasir F, Shabbir F, Babar ZUD, Saleem MF, Ullah K, Sun N, Ali F (2025) Supercapacitors: An Emerging Energy Storage System. Adv Energy Sustain Res 6(8): 2400412. https://doi.org/10.1002/aesr.202400412
3. Pal B, Yang S, Ramesh S, Thangadurai V, Jose R (2019) Electrolyte selection for supercapacitive devices: a critical review. Nanoscale Adv 1(10): 3807-3835. https://doi.org/10.1039/c9na00374f
4. Zhai Z, Zhang L, Du T, Ren B, Xu Y, Wang S, Miao J, Liu Z (2022) A review of carbon materials for supercapacitors. Mater Des 221: 111017. https://doi.org/10.1016/j.matdes.2022.111017
5. Yu X, Yan K, Zhou F, Liu G, Tian J, Zhuang C, Wang Y, Tian D (2026) Integrated design of electrospun cellulose-based 3D Co and CNT inserted porous carbon materials for supercapacitor and HER. Adv Compos Hybrid Mater 9(1): 8. https://doi.org/10.1007/s42114-025-01539-z
6. Manimekala T, Sivasubramanian R, Dar MA, Dharmalingam G (2025) Crafting the architecture of biomass-derived activated carbon via electrochemical insights for supercapacitors: a review. RSC Adv 15(4): 2490-2522. https://doi.org/10.1039/d4ra07682f
7. Tang Y, Smith Jr RL, Guo H, Qi X (2026) Advances in biomass-derived ordered mesoporous carbons. Adv Compos Hybrid Mater 9(2): 182. https://doi.org/10.1007/s42114-026-01698-7
8. Chen C, Hu L (2018) Nanocellulose toward Advanced Energy Storage Devices: Structure and Electrochemistry. Accounts Chem Res 51(12): 3154-3165. https://doi.org/10.1021/acs.accounts.8b00391

9. Yu Y, Li M, Zhou J, Sun M, Sun X, Jiang Z, Li Y, Wang C (2024) Structural designs of advanced wood-based thick electrodes for high-performance eco-supercapacitors. Nano Today 55: 102154. https://doi.org/10.1016/j.nantod.2024.102154
10. Wang F, Lee J, Chen L, Zhang G, He S, Han J, Ahn J, Cheong JY, Jiang S, Kim I-D (2023) Inspired by Wood: Thick Electrodes for Supercapacitors. ACS Nano 17(10): 8866-8898. https://doi.org/10.1021/acsnano.3c01241
11. Qu H, Fan L, Zhao C, Zhang J, Ji Y, Li C, Zhou X, Sheng L, Jiang L (2026) Hierarchical porous structure carbon electrodes derived from delignified wood with sulfuric acid-dispersed graphene for high-performance supercapacitors. J. Energy Storage 150: 120393. https://doi.org/10.1016/j.est.2026.120393
12. Zhu J, Xu Y, Wang J, Lin J, Sun X, Mao S (2015) The effect of various electrolyte cations on electrochemical performance of polypyrrole/RGO based supercapacitors. Phys Chem Chem Phys 17(43): 28666-28673. https://doi.org/10.1039/c5cp04080a
13. Jiang Y, Li J, Jiang Z, Shi M, Sheng R, Liu Z, Zhang S, Cao Y, Wei T, Fan Z (2021) Large-surface-area activated carbon with high density by electrostatic densification for supercapacitor electrodes. Carbon 175: 281-288. https://doi.org/10.1016/j.carbon.2021.01.016
14. Park KH, Park T, Yuk S, Ko B, Ahn J, Hong S-j, Lee D, Song SH (2023) Engineering Nanopores in Graphene-Based Nanoplatelets Derived from Cellulose-Based Biomass for High-Performance Capacitors. ACS Mater Lett 5(12): 3263-3272. https://doi.org/10.1021/acsmaterialslett.3c00831
15. Ferrari AC, Robertson J (2000) Interpretation of Raman spectra of disordered and amorphous carbon. Phys Rev B 61(20): 14095. https://doi.org/10.1103/PhysRevB.61.14095
16. Ferrari AC, Meyer JC, Scardaci V, Casiraghi C, Lazzeri M, Mauri F, Piscanec S, Jiang D, Novoselov KS, Roth S (2006) Raman Spectrum of Graphene and Graphene Layers. Phys Rev Lett 97(18): 187401. https://doi.org/10.1103/PhysRevLett.97.187401
17. Chen X, Wang X, Fang D (2020) A review on C1s XPS-spectra for some kinds of carbon materials. Fuller Nanotub Carbon Nanostruct 28(12): 1048-1058. https://doi.org/10.1080/1536383X.2020.1794851
18. Wang J, Kaskel S (2012) KOH activation of carbon-based materials for energy storage. J Mater Chem 22(45): 23710-23725. https://doi.org/10.1039/c2jm34066f
19. Huang Y, Ma E, Zhao G (2015) Thermal and structure analysis on reaction mechanisms during the preparation of activated carbon fibers by KOH activation from liquefied wood-based fibers. Ind Crop Prod 69: 447-455. https://doi.org/10.1016/j.indcrop.2015.03.002
20. Nanaji K, Sarada B, Varadaraju U, Rao TN, Anandan S (2021) A novel approach to synthesize porous graphene sheets by exploring KOH as pore inducing agent as well as a catalyst for supercapacitors with ultra-fast rate capability. Renew Energy 172: 502-513. https://doi.org/10.1016/j.renene.2021.03.039
21. Raymundo-Piñero E, Azaïs P, Cacciaguerra T, Cazorla-Amorós D, Linares-Solano A, Béguin F (2005) KOH and NaOH activation mechanisms of multiwalled carbon nanotubes with different structural organisation. Carbon 43(4): 786-795. https://doi.org/10.1016/j.carbon.2004.11.005
22. Wang Z, Lou B, Li J, Shi N, Yang X, Zhang J, Wu J, Wen F, Wang Y, Liu D (2025) Regulation of microcrystalline and pore structures in pitch-based hard carbon via liquid-phase crosslinking-assisted grain boundary etching to enhance sodium storage performance. J Mater Chem A 13(14): 10037-10048. https://doi.org/10.1039/d4ta08528k

23. Duay J, Sherrill SA, Gui Z, Gillette E, Lee SB (2013) Self-limiting electrodeposition of hierarchical MnO2 and M (OH) 2/MnO2 nanofibril/nanowires: mechanism and supercapacitor properties. ACS Nano 7(2): 1200-1214. https://doi.org/10.1021/nn3056077
24. Anusuya T, Kumar V (2023) Contribution of electron localization and delocalization zones in the performance of electrochemically reduced graphene oxide based supercapacitors: An experimental and the first-principles study. Carbon 215: 118481. https://doi.org/10.1016/j.carbon.2023.118481
25. Muthu RN, Tatiparti SSV (2020) Electrode and symmetric supercapacitor device performance of boron-incorporated reduced graphene oxide synthesized by electrochemical exfoliation. Energy Storage 2(4): e134. https://doi.org/10.1002/est2.134
26. Lindström H, Södergren S, Solbrand A, Rensmo H, Hjelm J, Hagfeldt A, Lindquist S-E (1997) Li+ ion insertion in TiO2 (anatase). 2. Voltammetry on nanoporous films. J Phys Chem B 101(39): 7717-7722. https://doi.org/10.1021/jp970490q
27. Wang R, Li Q, Cheng L, Li H, Wang B, Zhao X, Guo P (2014) Electrochemical properties of manganese ferrite-based supercapacitors in aqueous electrolyte: the effect of ionic radius. Colloid Surf A-Physicochem Eng Asp 457: 94-99. https://doi.org/10.1016/j.colsurfa.2014.05.059
28. Fic K, Lota G, Meller M, Frackowiak E (2012) Novel insight into neutral medium as electrolyte for high-voltage supercapacitors. Energy Environ Sci 5(2): 5842-5850. https://doi.org/10.1039/c1ee02262h
29. Moriwake H, Kuwabara A, Fisher CA, Ikuhara Y (2017) Why is sodium-intercalated graphite unstable? RSC Adv 7(58): 36550-36554. https://doi.org/10.1039/c7ra06777a
30. Wang Z, Selbach SM, Grande T (2014) Van der Waals density functional study of the energetics of alkali metal intercalation in graphite. RSC Adv 4(8): 4069-4079. https://doi.org/10.1039/c3ra47187j
31. Lu S, Song Y, Guo K, Chen X, Xu J, Zhao L (2018) Effect of aqueous electrolytes on the electrochemical behaviors of ordered mesoporous carbon composites after KOH activation as supercapacitors electrodes. J Electroanal Chem 818: 58-67. 10.1016/j.jelechem.2018.04.025
32. Wu H, Wang X, Jiang L, Wu C, Zhao Q, Liu X, Hu Ba, Yi L (2013) The effects of electrolyte on the supercapacitive performance of activated calcium carbide-derived carbon. J Power Sources 226: 202-209. https://doi.org/10.1016/j.jpowsour.2012.11.014
33. He X-j, Li X-j, Wang X-t, Zhao N, Yu M-x, Wu M-b (2014) Efficient preparation of porous carbons from coal tar pitch for high performance supercapacitors. New Carbon Mater 29(6): 493-502. https://doi.org/10.1016/S1872-5805(14)60150-5
34. Qu Q, Shi Y, Li L, Guo W-L, Wu Y, Zhang H, Guan S, Holze R (2009) V2O5· 0.6 H2O nanoribbons as cathode material for asymmetric supercapacitor in K2SO4 solution. Electrochem Commun 11(6): 1325-1328. https://doi.org/10.1016/j.elecom.2009.05.003

Supplementary Files

This is a list of supplementary files associated with this preprint. Click to download.

- supplementaryinformation.docx